

S-NPP Crosstrack Infra-red Sounder (CrIS) ESSPA-Ammonia (NH<sub>3</sub>)  
Retrieval Algorithm Theoretical Basis Document (ATBD)

Prepared by: Karen Cady-Pereira

Atmospheric and Environmental Research (AER)

Version 1

January 2020

## 1 Introduction

This document describes the algorithm for retrieving ammonia ( $\text{NH}_3$ ) profiles from the L1B radiances measured by the Cross Track Infrared Spectrometer (CrIS) currently flying aboard the Suomi National Polar-orbiting Partnership (SNPP) and Joint Polar Satellite System-1 (JPSS) satellites, and planned to be deployed on JPSS-2 and JPSS-3. The objective of these measurements is to create a global, long term  $\text{NH}_3$  dataset that can provide information on the temporal and spatial variability of  $\text{NH}_3$ . The data can also be used to estimate emissions and deposition, as well as to evaluate model performance and constrain model emissions.

The CrIS  $\text{NH}_3$  algorithm is directly derived from the NASA Tropospheric Emission Spectrometer (TES) operational algorithm (Shephard et al., 2011). A prototype version of the CrIS algorithm (Shephard and Cady-Pereira, 2015) has been extensively used to provide  $\text{NH}_3$  data over regions of interest these data have been used both for validation of CrIS  $\text{NH}_3$  and for demonstrating the many applications.

Section 2 describes the rationale for measuring  $\text{NH}_3$  from space, and showcases a number of results obtained from the TES operational algorithm and from the CrIS prototype algorithm. Section 3 describes the algorithm theoretical framework and the necessary inputs, and presents results from some simulated CrIS data.

## 2 $\text{NH}_3$ from space

### 2.1 Environmental impacts of $\text{NH}_3$

$\text{NH}_3$  is a highly reactive, short-lived air pollutant. Intended and unintended releases of  $\text{NH}_3$  into the environment over the last century have significantly altered the natural nitrogen cycle (Erismann et al., 2008).  $\text{NH}_3$  is emitted from a number of sources. The principal sources are agricultural and include waste from livestock and fertilizer application (EDGAR-Emission Database for Global Atmospheric Research, 2014). In urban areas automobiles with three-way catalytic converters (Sun et al., 2017) can be a major source of  $\text{NH}_3$ . For example, Nowak et al. (2012) estimate that in the Los Angeles basin cars contribute as much as 50% of the total  $\text{NH}_3$  emissions. Biomass burning events also generate large amounts of  $\text{NH}_3$  (Coheur et al., 2009, Whitburn et al., 2005, Whitburn et al., 2016). Recent *in-situ* measurements indicate that biomass burning may provide a large source of atmospheric nitrogen to sensitive high-elevation ecosystems in the western U.S. (Prenni et al., 2014).

Ammonia is the dominant base in the atmosphere, and plays a significant role in the formation of fine particulate matter ( $\text{PM}_{2.5}$ ) (e.g., Aneja et al., 2003), which can penetrate deep into the lungs and severely impact the respiratory and circulatory systems (Pope et al., 2009). Paulot and Jacob (2014) have recently shown that the costs associated with the health impacts of  $\text{NH}_3$  emitted from food production for export in the US more than offset the revenue from these exports.  $\text{PM}_{2.5}$  from  $\text{NH}_3$  increases aerosol optical depth, and as thus  $\text{NH}_3$  concentrations are climate-relevant as well (Pinder et al., 2012; Paulot et al., 2016). Ammonia is not yet a criteria pollutant in the US, but the EPA recently published new regulations

(<http://www.nsrlaw.com/single-post/2017/06/19/EPA-NSR-Chief-Outlines-NSR-Changes-at-2017-AWMA-Conference>) mandating that every state must set area specific significant emission rates (SERs) for NH<sub>3</sub>. NH<sub>3</sub> emissions are regulated by the European Union (EU) and it is a criteria pollutant in Canada.

Given the rapid growth of industrial-scale agriculture, due mainly to increase in egg, milk and meat consumption) especially in Asia (e.g. Xu et al., 2016), NH<sub>3</sub> emissions are projected to greatly increase over the next few decades in many parts of the world. Recent work by Warner et al. (2016) shows definite positive trends in NH<sub>3</sub> concentrations over the US, the EU and China, which the authors ascribe to declines in SO<sub>2</sub> and NO<sub>2</sub> emissions in all three regions due to more stringent controls. The reduction of NO<sub>x</sub> emissions will reduce the contribution of NO<sub>x</sub> to the deposition of reactive nitrogen, but Paulot et al. (2013) suggest that an increase in NH<sub>3</sub> emissions will likely compensate for this reduction.

The deposition of reduced nitrogen is already a major problem in the US. GEOS-Chem model results from Ellis et al. (2013) indicate that nitrogen deposition in US National Parks will be dominated by domestic NH<sub>3</sub> emissions by 2050. Nitrogen deposition already exceeds critical load (CL) values in the majority of US National Parks. When excess nitrogen is deposited to land it can severely degrade the ecosystems by stimulating different plant growth rates (Liu et al., 2013). NH<sub>3</sub> deposition to water bodies also contributes to algal blooms and hypoxia (Paerl et al., 2002, Paerl et al. 2014). Increased precipitation from climate change (Sinha et al., 2017) will likely exacerbate the latter effect.

## **2.2 Space based measurements**

Despite the growing recognition that NH<sub>3</sub> is an important pollutant, and that it will likely play a greater role in air quality and ecosystem health over the next decades, in situ measurements remain a challenge. NH<sub>3</sub> is easy to detect, but is hard to measure. There are many in situ techniques used to detect atmospheric NH<sub>3</sub> with varying time resolution and precision, but the main issue affecting precision is the inlet rather than the instrument. New open path sensors avoid this issue, but they cannot be deployed in many situations. NH<sub>3</sub> is sticky, and so it is challenging to get it into a given instrument quantitatively and quickly. These features are critical for characterizing the abundance of NH<sub>3</sub> in the background atmosphere, for making measurements of NH<sub>3</sub> fluxes, and deploying instruments on aircraft. Thus distribution, seasonality and emissions of NH<sub>3</sub> outside the range of a limited set of well-instrumented locations remain poorly constrained, reducing the accuracy with which models can represent concentrations and variability. For example, Schiferl et al. (2016) found that GEOS-Chem generally underrepresented NH<sub>3</sub> and did not reproduce the summer interannual variability in the US. Bottom up inventories often underestimate emissions due to scaling difficulties (Walker et al., 2012).

Satellite data, in spite of their associated uncertainties, provide by virtue of their spatial and temporal density another option for mapping NH<sub>3</sub> distribution and quantifying emissions. A number of examples illustrating the capabilities and applications of satellite NH<sub>3</sub> follow.

TES NH<sub>3</sub> data are extremely sparse and thus difficult to validate. Nevertheless, Pinder et al. (2011) measured similar temporal and spatial variability from TES NH<sub>3</sub> and surface CAMNet NH<sub>3</sub> measurements in North Carolina during 2009. Shephard et al. (2015) showed good agreement between NH<sub>3</sub> from TES and from an Aerodyne Quantum Cascade Laser (QCL) mounted on an aircraft during the intensive field campaign in 2013 in support of the Joint Canada–Alberta Implementation Plan for Oil Sands Monitoring (JOSM). Measurements taken during the California DISCOVER-AQ campaign (Figure 1, left) demonstrate the ability of both TES and CrIS data to capture the spatial variability of NH<sub>3</sub> obtained from aircraft instruments, as well as the good agreement between the two satellite sensors. May 2012 CrIS NH<sub>3</sub> means over the western US (Figure 1, right) show expected “hotspots” in regions of intense agricultural activity: the Central Valley, the Imperial Valley and the Snake River valley. More systematic validation was carried out by Dammers et al. (2017), using Fourier Transform Infrared Spectrometer (FTIR) instruments from seven sites of the Network for the Detection of Atmospheric Composition Change (NDACC). Overall FTIR and CrIS total columns have a positive correlation of 0.77 with very little bias, though CrIS tends to slightly overestimate low concentrations near its detection limit (Figure 2). Separate analysis suggests that this pattern may possibly be explained by sampling differences, as CrIS has a 14-km diameter footprint at nadir, while the FTIR essentially makes a point observation.

Further validation has been done against data from aircraft spirals taken during the Deriving Information on Surface Conditions from Column and VERTically. Resolved Observations Relevant to Air Quality (DISCOVER-AQ) campaign in California in January and February 2013 (Figure 3). CrIS NH<sub>3</sub> profiles were compared against data from both the Picarro and PTR-ToF-MS instruments flying aboard the NASA P3B. The results from the PTR comparison are shown in Figure 3 (results from the Picarro were very similar); when the CrIS operator is applied to the PTR data, the retrievals show no bias (dark green bars), indicating that the retrievals are performing as well as possible. When the CrIS operator is not applied, the CrIS retrievals show a marked low bias at the surface, and a slight negative bias at 900 mbar. This is not unexpected, as the averaging kernel shows low sensitivity at the surface. We are investigating two approaches to increase the sensitivity at the lowest levels: loosening the constraint and increasing the number of retrieval levels; however, given the limited information in the signal, increased sensitivity may come at the cost of increased errors.

In spite of the sparseness of the TES data, Zhu et al. (2013) have demonstrated that TES NH<sub>3</sub> data over North America in the 2006–2009 period could be used in an inverse modeling framework to constrain emissions sufficiently to improve agreement between GEOS-Chem output and surface measurements from the National Atmospheric Deposition Program (NADP) Ammonia Monitoring Network (AMoN) network (Figure 4).

Dry deposition of reactive nitrogen can be estimated by combining NH<sub>3</sub> from CrIS and NO<sub>2</sub> (from the Ozone Mapping Instrument (OMI) data and deposition velocity from a model. The ratio of NH<sub>3</sub> to NO<sub>2</sub> deposition over North America (Figure 5) shows that NH<sub>3</sub> dominates the deposition of reactive nitrogen over most of the continent, except in some metropolitan areas (Kharol et al., 2017). Since the concentrations of NO<sub>2</sub> are decreasing due to stricter controls, it

is expected that NH<sub>3</sub> will increasingly determine Nr deposition everywhere.

### 3 SNPP Algorithm

#### 3.1 Optimal estimation

The CrIS NH<sub>3</sub> algorithm delivered to the NASA SIPS implements an optimal estimation (OE) approach (Rodgers, 2000) that seeks to reduce the difference between the measured CrIS radiances in the NH<sub>3</sub> ν<sub>2</sub> vibrational band centered around 950 cm<sup>-1</sup> (Beer et al., 2008) and the calculated radiances from a forward model. This is the approach followed by the TES team, and this, along with the adoption of the same a-priori profiles and constraints, will ensure the creation of a long-term data set consistent with TES. Furthermore, OE provides the averaging kernels and error estimates that are essential for characterizing the amount of information and the error in the retrieved profiles, and for ingesting these profiles in inverse modeling, as the NPP sounding group evaluation report (<http://npp.gsfc.nasa.gov/teaminfo.html>) has noted.

Since the retrieval is non-linear, an a priori constraint is used for estimating the true state (Bowman et al., 2006). If the estimated (retrieved) state is close to the actual state, then the estimated state can be expressed in terms of the actual state through the linear retrieval (Rodgers, 2000):

$$\hat{\mathbf{x}} = \mathbf{x}_a + \mathbf{A}(\mathbf{x} - \mathbf{x}_a) + \mathbf{G}\mathbf{n} + \mathbf{G}\mathbf{K}_b(\mathbf{b} - \mathbf{b}_a) \quad (1)$$

where  $\hat{\mathbf{x}}$ ,  $\mathbf{x}_a$ , and  $\mathbf{x}$  are the retrieved, a priori, and the “true” state vectors respectively. The gain matrix,  $\mathbf{G}$ , maps from spectral radiance space into retrieval parameter space, and the vector  $\mathbf{n}$  represents the noise on the measured spectral radiances. The vector  $\mathbf{b}$  represents the true state for other parameters that are not measured in the NH<sub>3</sub> retrieval itself, but that may nonetheless impact these species retrievals results (e.g., concentrations of interfering gases, calibration, etc.). The vector  $\mathbf{b}_a$  contains the corresponding a priori values, and  $\mathbf{K} = \partial \mathbf{L} / \partial \mathbf{b}$  is a Jacobian describing the dependence of the forward model radiances  $\mathbf{L}$  on the parameters in vector  $\mathbf{b}$ .

The averaging kernel,  $\mathbf{A}$ , describes the sensitivity of the retrieval to the true state:

$$\mathbf{A} = \frac{\partial \hat{\mathbf{x}}}{\partial \mathbf{x}} = (\mathbf{K}^T \mathbf{S}_n^{-1} \mathbf{K} + \mathbf{S}_a^{-1})^{-1} \mathbf{K}^T \mathbf{S}_n^{-1} \mathbf{K} = \mathbf{G}\mathbf{K} \quad (2)$$

where  $\mathbf{S}_n$  is the instrument noise covariance matrix, and  $\mathbf{S}_a$  is the a priori covariance matrix for the retrieval. The Jacobian,  $\mathbf{K}$ , is the sensitivity of the forward model radiances to the true state vector,  $\mathbf{K} = \partial \mathbf{L} / \partial \mathbf{x}$ .

The rows of  $\mathbf{A}$  are functions (often Gaussian in shape for nadir infrared observations) with a finite width corresponding to the vertical resolution of the retrieved parameter. The sum of each row of  $\mathbf{A}$  provides a measure of the fraction of retrieval information that comes from the

measurement rather than the a priori (Rodgers, 2000) at the corresponding altitude, provided that the retrieval quasi-linear. The trace of the averaging kernel matrix gives the number of degrees of freedom for signal (DOFS) from the retrieval.

The total error covariance matrix  $\mathbf{S}_x$  for a given retrieved parameter  $\hat{x}$  is given by:

$$\mathbf{S}_x = (\mathbf{A} - \mathbf{I})\mathbf{S}_a(\mathbf{A} - \mathbf{I})^T + \mathbf{G}\mathbf{S}_n\mathbf{G}^T + \mathbf{G}\mathbf{K}_b\mathbf{S}_b(\mathbf{G}\mathbf{K}_b)^T \quad (3)$$

where  $\mathbf{S}_b$  is the expected covariance of the non-retrieved parameters. The total error for a retrieved profile is expressed as the sum of: *i*) the smoothing errors (first term on the right-hand-side), i.e. the uncertainty due to unresolved fine structure in the profile; *ii*) the measurement errors (second term) originating from random noise in the spectrum; and *iii*) the systematic errors (last term) due to uncertainties in the non-retrieved forward model parameters, some of which are constant and some of which change from retrieval-to-retrieval (Worden et al., 2004). For the current CrIS  $\text{NH}_3$  algorithm this last term is not calculated and is not included in the total error estimate. By providing the expected error covariance and the averaging kernels, this approach facilitates the use of the retrieved profiles in inverse modeling efforts.

### 3.2 Forward model

AER's fast and accurate radiative transfer algorithm Optimal Spectral Sampling (OSS) model (Moncet et al., 2008) has been chosen as forward model for these retrievals. The Optimal Spectral Sampling (OSS) method was designed specifically for the modeling of radiances measured by sounding radiometers in the infrared (Moncet et al., 2008), although it is applicable throughout the microwave, visible, and ultraviolet regions. It has been implemented in the Joint Center for Satellite Data Assimilation (JCSDA) Community Radiative Transfer Model (CRTM). The OSS approach is an extension of the exponential sum fitting of transmittances technique in that channel-average radiances are obtained from a weighted sum of monochromatic calculations. Among the advantages of the OSS method is that its numerical accuracy, with respect to a reference line-by-line model, is selectable, allowing the model to provide whatever balance of accuracy and computational speed is optimal for a particular application. Generally only a few monochromatic points are required to model channel radiances with a brightness temperature accuracy of 0.05 K, and greater accuracies are easily achieved. Note these modeled radiances already contain the response of the instrument, so that no instrument line shape (ILS) needs to be applied to the output.

This version of using the OSS model has been optimized for the CrIS spectral channels by Jean-Luc Moncet of AER (Moncet et al., 2008). This model is trained using AER's state-of-the-science high-resolution Line-By-Line Radiative Transfer Model (LBLRTM; Clough et al., 2005), which is recognized as a reference standard for the inter-comparison of radiative transfer models in the thermal IR (Forster et al., 2011; Oreopoulos et al., 2012). LBLRTM is the foundation for the TES satellite retrieval algorithms (Clough et al., 2006) as well as for IASI (Amato et al., 2002; Tjemkes

et al., 2003). The performance of LBLRTM v12.1 in the thermal infrared was recently validated using a global data set of 120 spectra measured with IASI (Alvarado et al., 2013). The current version of OSS for CrIS was built with LBLRTM v12.4 and the AER V.3.4 line parameters, except for CO<sub>2</sub>, for which parameters from AER V3.4.1 were used.

### 3.3 Retrieval Code: ESSPA

### 3.4 Algorithm setup

#### 3.4.1 Microwindows and noise error

In order to reduce the impact of interfering species, the CrIS NH<sub>3</sub> retrieval uses a limited number of spectral points, which has the added advantage of reducing the computational burden of high-spectral resolution forward model calculations, and the storage size of output retrieval parameters (i.e. Jacobians, averaging kernels, error covariances). The spectral points are listed below, in units of cm<sup>-1</sup>:

962.5, 963.125, 963.75, 964.375, 965.0, 965.625, 966.25, 966.875, 967.5, 968.125, 968.75

The noise error covariance matrix is treated as a diagonal matrix, whose values come directly from the L1B data. Thus no correlation is assumed between the channels.

#### 3.4.2 A priori and constraint selection

Since the NH<sub>3</sub> concentrations can vary by orders of magnitude in time and space, and are not well known globally from scene-to-scene, a single a priori will not yield reasonable results for all scenes: the solution space is too large to be explored without some constraint on the retrieval. The a priori selection algorithm is similar but not identical to that developed for TES. The selection algorithm uses an on-line (@967.5 cm<sup>-1</sup>) off-line (@981.25 cm<sup>-1</sup>) difference in brightness temperature to estimate the strength of the NH<sub>3</sub> signal; this value is then used to select one of three a priori profiles and constraint matrices. The a priori profiles and constraints are the same as those built for the TES NH<sub>3</sub> retrievals (Shephard et al., 2011). Both are derived from global distributions of NH<sub>3</sub> from the chemical transport model GEOS-Chem (Zhu et al., 2013) for three categories of NH<sub>3</sub> profiles (Figure 6):

- *Polluted*: all profiles with surface NH<sub>3</sub> ≥ 5 ppbv.
- *Moderately polluted*: all profiles with 1 ppbv ≤ NH<sub>3</sub> < 5 ppbv at the surface or NH<sub>3</sub> < 1 ppbv at the surface, but NH<sub>3</sub> > 1 ppbv between the surface and 500 hPa; this profile type seeks to represent those cases in which the local emissions are less important than the transport into the region
- *Unpolluted*: all profiles with NH<sub>3</sub> < 1 ppbv between the surface and 800 hPa.

The diagonals of the covariance matrices are the basis for generating the constraint matrix used in the retrievals. The diagonal values (e.g., the expected variances) were modified to reflect the sensitivity of the TES instrument: where there is little ammonia and no TES sensitivity, e.g.,

above 400 hPa, the constraint is very tight. The off-diagonals of the constraint matrix were generated with a 1-km correlation length.

Both the TES operational algorithm and the CrIS prototype algorithm added a vertical shift to the selected a priori profile for scenes with elevation. The objective was to ensure that the profile shape did not get truncated. The ESSPA code instead uses a hybrid sigma-pressure grid, and the a priori profiles are stored on this grid, which obviates the need for shifting and is a much more robust approach.

### 3.4.3 Retrieval inputs

Due to the high spatial variability of  $\text{NH}_3$  the retrievals are carried out on the non-cloud-cleared L1B radiances from each Field-of-View (FOV). The retrieval also requires temperature and water vapor profiles, as well as surface temperature and emissivity, which will be obtained from L2 products. The current L2 products are generated on the much coarser Field-of-Regard (FOR) resolution. While the  $\text{NH}_3$  retrieval is only moderately sensitive to errors in water vapor and air temperature, it is very sensitive to errors in surface emission. Therefore each  $\text{NH}_3$  retrieval is preceded by a refinement of the surface temperature and emissivity through a retrieval on the FOV resolution.

Since  $\text{NH}_3$  is principally concentrated in the boundary layer, and frequently peaks at ground level, it cannot be detected in cloudy scenes. The BT difference test used to determine the a priori will usually flag these pixels as unpolluted. Cold pixels are also flagged as unpolluted. In our prototype algorithm, the retrieval is skipped for these pixels.

### 3.4.4 Retrieval outputs and evaluation

The retrieval generates  $\text{NH}_3$  profiles, error matrices and averaging kernels. The current ESSPA implementation was first tested on simulated radiances generated by running OSS on a set of  $\text{NH}_3$  profiles obtained from the prototype CrIS  $\text{NH}_3$  retrieval during the Southeast Nexus (SENEX) campaign in 2013. On average the ESSPA retrievals were biased low by 0.5 to 1.0 ppbv below 925 mbar, with the bias decreasing to zero above that level: at first because the CrIS sensitivity increased and then due to the stronger constraints and low levels of  $\text{NH}_3$ .



## Tables and Figures

Table 1: SNR values and corresponding a priori profiles

SNR value	Selected a priori
SNR<-6.0	Polluted
SNR>-6.0 AND SNR<-2.0	Moderate
SNR<-2.0 AND SNR>1.0	Unpolluted
SNR>1.0 AND SNR<3.0	Moderate
SNR>3.0	Polluted

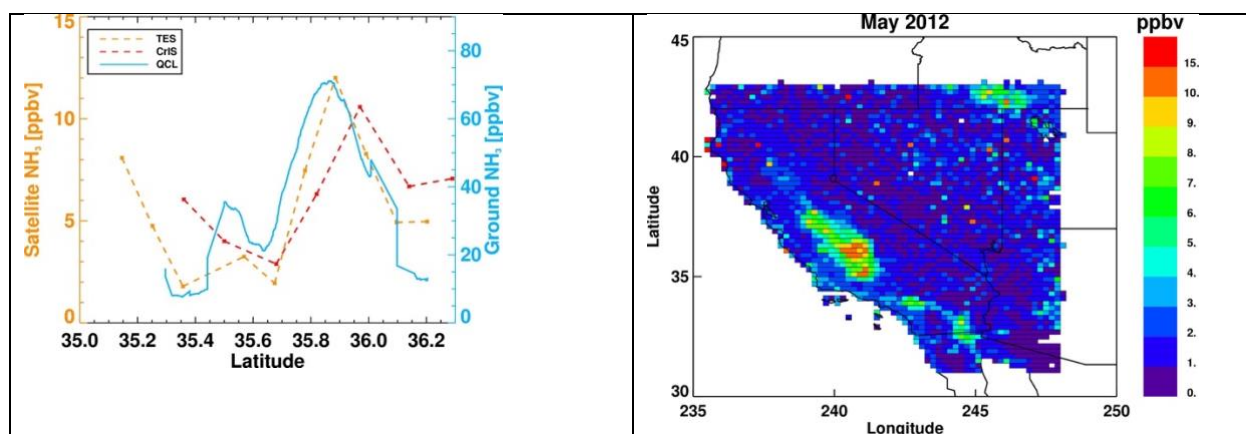


Figure 1: Left: Satellite (TES and CrIS) and ground based  $\text{NH}_3$  (QCL) measurements along the TES track in during DAQ-California in 2013; these data are from January 28, 2013. Right: mean CrIS  $\text{NH}_3$  over westernmost US for May 2012.

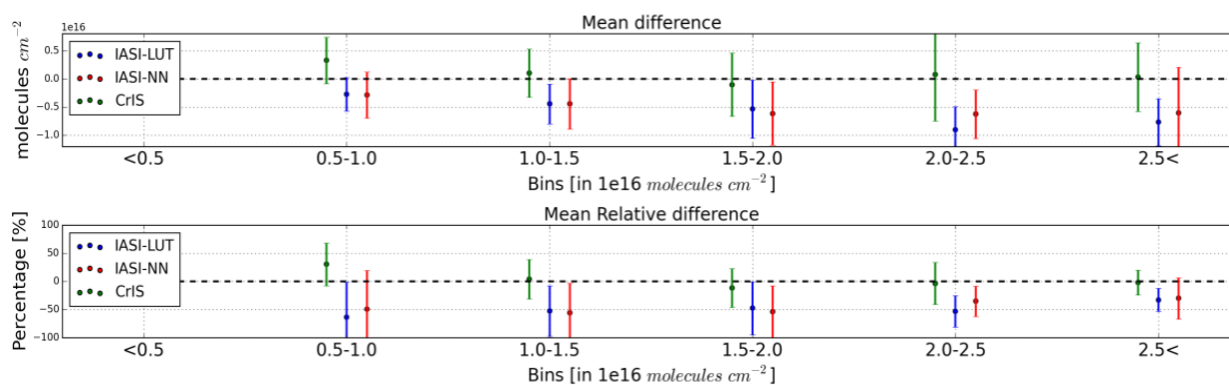


Figure 2: Top: Mean differences between satellite and surface FTIR  $\text{NH}_3$  column amounts, binned by amount. Bottom: Percent difference of same parameters.

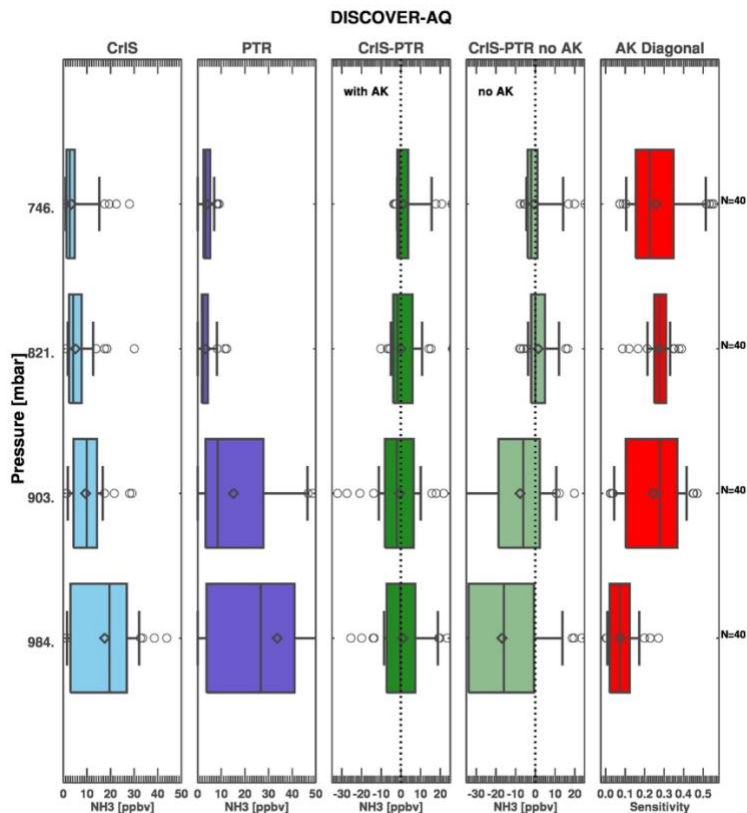


Figure 3:  $\text{NH}_3$  profiles statistics from the California DISCOVER-AQ campaign (January-February 2013): mean CrIS  $\text{NH}_3$  (blue), mean PTR  $\text{NH}_3$  (purple), mean CrIS-PTR difference with CrIS operator applied (dark green), mean CrIS-PTR difference with no CrIS operator (light green), mean diagonal values of the CrIS averaging kernel (red). Each box represents the 25<sup>th</sup> to 75<sup>th</sup> percentile, bars extend to 10<sup>th</sup> and 90<sup>th</sup> percentile; circles, diamonds and vertical bars indicate outliers, mean values and median values respectively.

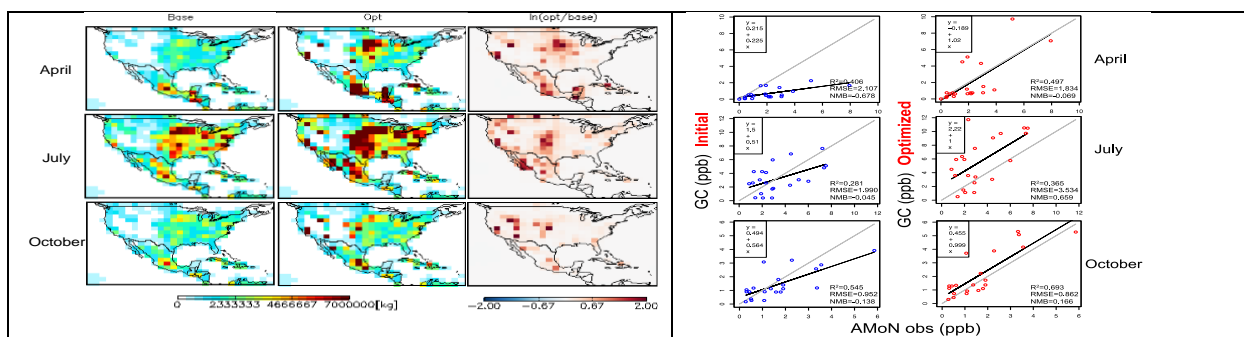


Figure 4: Left:  $\text{NH}_3$  emissions from GEOS-Chem before and after the assimilation of TES data. Right: Comparison of  $\text{NH}_3$  Representative Volume Mixing Ratio (RVMR) from TES and GEOS-Chem before and after the assimilation (see Zhu et al., 2013).

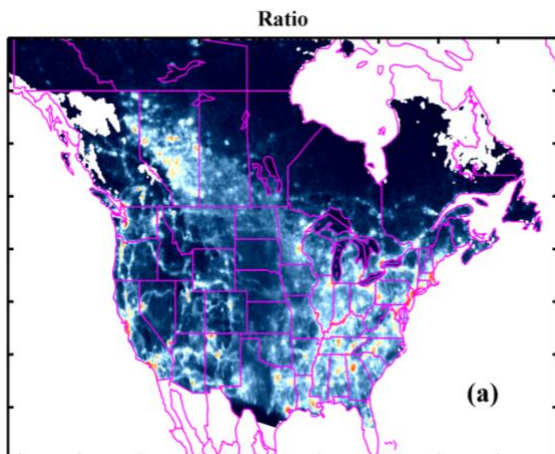


Figure 5: Ratio of nitrogen dioxide ( $\text{NO}_2$ ) to total  $\text{Nr}$  ( $\text{NH}_3 + \text{NO}_2$ ) dry deposition flux over North America. The yellow-to-red areas indicate where the dry deposition of  $\text{Nr}$  ( $\text{NH}_3 + \text{NO}_2$ ) has a greater contribution from  $\text{NO}_2$ , whereas the blue regions indicate dominant  $\text{NH}_3$  dry deposition (see Kharol et al., 2017).

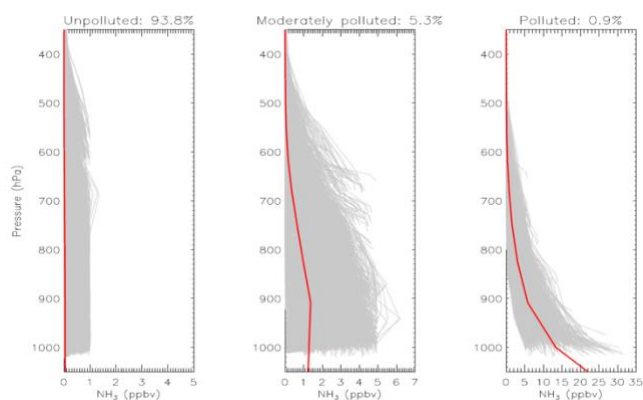


Figure 6: Monthly means of GEOS-Chem 2005  $\text{NH}_3$  simulations, grouped as described in section 3.4.2. Left: unpolluted, middle: moderate, right: polluted. Red curves are means of each set and are the a priori profiles used in the algorithm.

## References

- Alvarado, M. J., Payne, V. H., Mlawer, E. J., Uymin, G., Shephard, M. W., Cady-Pereira, K. E., Delamere, J. S., and Moncet, J.-L.: Performance of the line-by-line radiative transfer model (LBLRTM) for temperature, water vapor, and trace gas retrievals: recent updates evaluated with IASI case studies, *Atmos. Chem. Phys. Discuss.*, 13, 79-144, doi:10.5194/acpd-13-79-2013, 2013.
- Amato, U., Masiello, G., Serio, C., and Viggiano, M. (2002), The  $\sigma$ -IASI code for the calculation of infrared atmospheric radiance and its derivatives, *Environmental Modelling & Software*, 17, 651-667, doi:10.1016/S1364-8152(02)00027-0.
- Aneja, V. P., D. R. Nelson, P. A. Roelle, J. T. Walker, and W. Battye, Agricultural ammonia emissions and ammonium concentrations associated with aerosols and precipitation in the southeast United States, *J. Geophys. Res.*, 108(D4), 4152, doi:10.1029/2002JD002271, 2003.

- Beer, R., Shephard M. W., Kulawik, S. S., Clough, S. A., Eldering, A., Bowman, K. W., Sander, S. P., Fisher, B. M., Payne, V. H., Luo, M., Osterman, G. B., and Worden, J. R.: First satellite observations of lower tropospheric ammonia and methanol, *Geophys. Res. Lett.*, 35, L09801, doi:10.1029/2008GL033642, 2008.
- Bowman, K. W., Rodgers C. D., Sund-Kulawik S., Worden J., Sarkissian E., Osterman G., Steck T., Luo M., Eldering A., Shephard M. W., Worden H., Clough S. A., Brown P. D., Rinsland C. P., Lampel M., Gunson M., and Beer R.: Tropospheric emission spectrometer: Retrieval method and error analysis, *IEEE Trans. Geosci. Remote Sens.*, 44(5), 1297–1307, doi:10.1109/TGRS.2006.871234, 2006.
- Clough, S. A., Shephard M. W., Mlawer, E. J., Delamere, J. S., Iacono, M. J., Cady-Pereira, K., Boukabara, S., and Brown, R.D.: Atmospheric radiative transfer modeling: a summary of the AER codes, *J. Quant. Spectrosc. Radiat. Transfer*, 91, 233-244, 2005.
- Coheur, P.-F., Clarisse, L., Turquety, S., Hurtmans, D., and Clerbaux, C. (2009) IASI measurements of reactive trace species in biomass burning plumes. *Atmos. Chem. Phys.*, 9, 5655–5667.
- Dammers, E., Shephard, M. W., Palm, M., Cady-Pereira, K., Capps, S., Lutsch, E., Strong, K., Hannigan, J. W., Ortega, I., Toon, G. C., Stremme, W., Grutter, M., Jones, N., Smale, D., Siemons, J., Hrpcek, K., Tremblay, D., Schaap, M., Notholt, J., and Erisman, J. W.: Validation of the CrIS Fast Physical NH<sub>3</sub> Retrieval with ground-based FTIR, *Atmos. Meas. Tech.*, 10, 2645-2667, <https://doi.org/10.5194/amt-10-2645-2017>, 2017.
- Ellis, R. A., Jacob, D. J., Sulprizio, M. P., Zhang, L., Holmes, C. D., Schichtel, B. A., Blett, T., Porter, E., Pardo, L. H., and Lynch, J. A.: Present and future nitrogen deposition to national parks in the United States: critical load exceedances, *Atmos. Chem. Phys.*, 13, 9083-9095, <https://doi.org/10.5194/acp-13-9083-2013>, 2013.
- Erisman, J. W., M. A. Sutton, J. Galloway, Z. Klimont, and W. Winiwarter (2008), How a century of ammonia synthesis changed the world, *Nature Geosci.*, 1(10), 636-639.
- Forster, P. M., Fomichev, V. I., Rozanov, E., Cagnazzo, C., Jonsson, A. I., Langematz, U., Fomin, B., Iacono, M. J., Mayer, B., Mlawer, E., Myhre, G., Portmann, R. W., Akiyoshi, H., Falaleeva, V., Gillett, N., Karpechko, A., Li, J., Lemennais, P., Morgenstern, O., Oberländer, S., Sigmond, M., and Shibata, K. (2011), Evaluation of radiation scheme performance within chemistry climate models, *J. Geophys. Res.*, 116, D10302, doi:10.1029/2010JD015361.
- Kharol, S. K., Shephard, M. W., McLinden, C. A., Zhang, L., Sioris, C. E., O'Brien, J. M.,... Krotkov, N. A.: Dry deposition of reactive nitrogen from satellite observations of ammonia and nitrogen dioxide over North America. *Geophysical Research Letters*, 44. <https://doi.org/10.1002/2017GL075832>, 2017
- Moncet, J.-L., Uymin G., Lipton A. E., and Snell H. E.: Infrared radiance modeling by optimal spectral sampling. *J. Atmos. Sci.*, 65, 3917-3934, 2008.
- Nowak, J. B., Neuman, J. A., Bahreini, R., Middlebrook, A. M., Holloway, J. S., McKeen, S. A., (2012): Ammonia sources in the California South Coast Air Basin and their impact on ammonium nitrate formation. *Geophysical Research Letters*, 39(7).
- Oreopoulos, L., Mlawer, E., Delamere, J., Shippert, T., Cole, J., Fomin, B., Iacono, M., Jin, Z., Li, J., Manners, J., Räisänen, P., Rose, F., Zhang, Y., Wilson, M. J., and Rossow, W. (2012), The Continual Intercomparison of Radiation Codes: Results from phase I, *J. Geophys. Res.*, 117, D06118, doi:10.1029/2011JD016821.

- Paerl, H.W., W. S. Gardner, M. J. McCarthy, B. L. Peierls, and S. W. Wilhelm: Algal blooms: Noteworthy nitrogen, *Science*, 346 (6206), 175, doi: 10.1126/science.346.6206.175a, 2014
- Paerl, H., R. Dennis, and D. Whittall: Atmospheric deposition of nitrogen: Implications for nutrient over-enrichment of coastal waters, *Estuaries*, 25(4), 677–693, 2002.
- Paulot, R., [P. Ginoux](#), [W. F. Cooke](#), [L. J. Donner](#), [S.-M. Fan](#), [M. Lin](#), J. Mao, [V. Naik](#), and [L. W. Horowitz](#) (2016), Sensitivity of nitrate aerosols to ammonia emissions and to nitrate chemistry: implications for present and future nitrate optical depth. *Atmospheric Chemistry and Physics*, 16(3), DOI:[10.5194/acp-16-1459-2016](#) .
- Paulot, F., & Jacob, D. J: Hidden cost of US agricultural exports: particulate matter from ammonia emissions. *Environmental science & technology*, 48 (2), 903-908, 2014.
- Paulot, F., Jacob, D. J., & Henze, D. K.: Sources and processes contributing to nitrogen deposition: an adjoint model analysis applied to biodiversity hotspots worldwide. *Environmental science & technology*, 47(7), 3226-3233, 2013.
- Pinder, R. W., Davidson, E. A., Goodale, C. L., Greaver, T. L., Herrick, J. D., & Liu, L. (2012). Climate change impacts of US reactive nitrogen. *Proceedings of the National Academy of Sciences*, 109(20), 7671-7675.
- Pinder, R. W., Walker, J. T., Bash, J. O., Cady-Pereira, K. E., Henze, D. K., Luo, M., and Shephard, M. W. (2011), Quantifying spatial and temporal variability in atmospheric ammonia with in situ and space-based observations, *Geophys. Res. Lett.*, 38, L04802, doi:10.1029/2010GL046146.
- Pope, C., III; Ezzati, M.; Dockery, D. W. (2009), Fine-particulate air pollution and life expectancy in the United States *N. Engl. J. Med.*, 360, 376–386.
- Prenni, A. J., E. J. T. Levin, K. B. Benedict, A. P. Sullivan, M. I. Schurman, K. A. Gebhart, D. E. Day, C. M. Carrico, W. C. Malm, B. A. Schichtel, J. L. Collett Jr, and S. M. Kreidenweis (2014), Gas-phase reactive nitrogen near Grand Teton National Park: Impacts of transport, anthropogenic emissions, and biomass burning, *Atmospheric Environment*, 89, 749-756, <http://dx.doi.org/10.1016/j.atmosenv.2014.03.017>.
- Rodgers, C. D.: Inverse methods for atmospheric Sounding: Theory and Practice, World Sci., Hackensack, N. J., 2000.
- Schiferl, L. D., C. L. Heald, J. B. Nowak, J. S. Holloway, J. A. Neuman, R. Bahreini, I. B. Pollack, T. B. Ryerson, C. Wiedinmyer, and J. G. Murphy (2014), An investigation of ammonia and inorganic particulate matter in California during the CalNex campaign, *Journal of Geophysical Research: Atmospheres*, 119(4), 1883-1902, 10.1002/2013JD020765.
- Shephard, M. W. and K.E. Cady-Pereira: Cross-track Infrared Sounder (CrIS) satellite observations of tropospheric ammonia, *Atmos. Meas. Tech.*, 8, 1323-1336, doi:10.5194/amt-8-1323-2015, 2015.
- Shephard, M. W., McLinden, C. A., Cady-Pereira, K. E., Luo, M., Moussa, S. G., Leithead, A., Liggio, J., Staebler, R. M., Akingunola, A., Makar, P., Lehr, P., Zhang, J., Henze, D. K., Millet, D. B., Bash, J. O., Zhu, L., Wells, K. C., Capps, S. L., Chaliyakunnel, S., Gordon, M., Hayden, K., Brook, J. R., Wolde, M., and Li, S.-M.: Tropospheric Emission Spectrometer (TES) satellite observations of ammonia, methanol, formic acid, and carbon monoxide over the Canadian oil sands: validation and model evaluation, *Atmos. Meas. Tech.*, 8, 5189-5211, <https://doi.org/10.5194/amt-8-5189-2015>, 2015.
- Shephard, M. W., K. E. Cady-Pereira, M. Luo, D.K. Henze, R.W. Pinder, J.T Walker, C.P. Rinsland,

- J.O. Bash, L. Zhu, V. Payne, and L. Clarisse (2011), TES Ammonia Retrieval Strategy and Global Observations of the Spatial and Seasonal Variability of Ammonia, *Atmos. Chem. Phys.*, 11, 10743–10763, doi:10.5194/acp-11-10743-2011
- Sinha, E., Michalak, A.M. and V. Balaji: Eutrophication will increase during 21st century as a result of precipitation changes, *Science*, 357, 6349, 405-408, 2017.
- Sun, K., Lei Tao, David J. Miller, Da Pan, Levi M. Golston, Mark A. Zondlo, Robert J. Griffin, H. W. Wallace, Yu Jun Leong, M. Melissa Yang, Yan Zhang, Denise L. Mauzerall, and Tong Zhu: Vehicle Emissions as an Important Urban Ammonia Source in the United States and China, *Environmental Science & Technology*, 51 (4), 2472-2481 DOI: 10.1021/acs.est.6b02805, 2017.
- Tjemkes, S. A., Patterson, T., Rizzi, R., Shephard, M. W., Clough, S. A., Matricardi, M., Haigh, J. D., Höpfner, M., Payan, S., Trotsenko, A., Scott, N., Rayer, P., Taylor, J. P., Clerbaux, C., Strow, L. L., DeSouza-Machado, S., Tobin, D., Knuteson, R. (2003), The ISSWG line-by-line inter-comparison experiment, *Journal of Quantitative Spectroscopy and Radiative Transfer*, 77, 433-453, 10.1016/S0022-4073(02)00174-7.
- Walker, J. M., S. Philip, R. V. Martin, and J. H. Seinfeld, Simulation of nitrate, sulfate, and ammonium aerosols over the united states, *Atmos. Chem. Phys.*, 12, 11,213{11,227, doi:10.5194/acp-12-11213-2012, 2012.
- Warner, J. X., R. R. Dickerson, Z. Wei, L. L. Strow, Y. Wang, and Q. Liang (2017), Increased atmospheric ammonia over the world's major agricultural areas detected from space, *Geophys. Res. Lett.*, 44, doi:10.1002/2016GL072305.
- Whitburn, S., M. Van Damme, J. W. Kaiser, G. R. van der Werf, S. Turquety, D. Hurtmans, L. Clarisse, C. Clerbaux, and P. F. Coheur, Ammonia emissions in tropical biomass burning regions: Comparison between satellite-derived emissions and bottom up \_re inventories, *Atmos. Environ.*, 121, 42\_54, 2015.
- Whitburn, S., M. Van Damme, L. Clarisse, S. Turquety, C. Clerbaux, and P.-F. Coheur, Doubling of annual ammonia emissions from the peat fires in Indonesia during the 2015 El Niño, *Geophys. Res. Lett.*, 43, 2016GL070,620, 2016.
- Worden, J., Kulawik S. S., Shephard M. W., Clough S. A., Worden H., Bowman K., and Goldman A.: Predicted errors of tropospheric emission spectrometer nadir retrievals from spectral window selection, *J. Geophys. Res.*, 109, D09308, doi:10.1029/2004JD004522, 2004.
- Xu, P., Y. J. Liao, Y. H. Lin, C. X. Zhao, C. H. Yan, M. N. Cao, G. S. Wang, and S. J. Luan (2016) High-resolution inventory of ammonia emissions from agricultural fertilizer in China from 1978 to 2008, *Atmos. Chem. Phys.*, 16, 1207 -1218, doi:10.5194/acp-16-1207-2016.
- Zhu, L., D. K. Henze, K. E. Cady-Pereira, M. W. Shephard, M. Luo, R. W. Pinder, J. O. Bash, and G.-R. Jeong (2013), Constraining U.S. ammonia emissions using TES remote sensing observations and the GEOS-Chem adjoint model, *J. Geophys. Res. Atmos.*, 118, doi:10.1002/jgrd.50166.